

Journal Pre-proofs

Stable and efficient self-sustained photoelectrochemical desalination based on CdS QDs/BiVO₄ heterostructure

Mengjun liang, Jiancong Zhang, Karthick Ramalingam, Qiang Wei, Kwan San Hui, Su Htike Aung, Kwun Nam Hui, Fuming Chen

PII: S1385-8947(21)03747-5
DOI: <https://doi.org/10.1016/j.cej.2021.132168>
Reference: CEJ 132168

To appear in: *Chemical Engineering Journal*

Received Date: 23 April 2021
Revised Date: 13 August 2021
Accepted Date: 28 August 2021

Please cite this article as: M. liang, J. Zhang, K. Ramalingam, Q. Wei, K. San Hui, S. Htike Aung, K. Nam Hui, F. Chen, Stable and efficient self-sustained photoelectrochemical desalination based on CdS QDs/BiVO₄ heterostructure, *Chemical Engineering Journal* (2021), doi: <https://doi.org/10.1016/j.cej.2021.132168>

This is a PDF file of an article that has undergone enhancements after acceptance, such as the addition of a cover page and metadata, and formatting for readability, but it is not yet the definitive version of record. This version will undergo additional copyediting, typesetting and review before it is published in its final form, but we are providing this version to give early visibility of the article. Please note that, during the production process, errors may be discovered which could affect the content, and all legal disclaimers that apply to the journal pertain.

© 2021 Elsevier B.V. All rights reserved.



Stable and efficient self-sustained photoelectrochemical desalination based on CdS QDs/BiVO₄ heterostructure

Mengjun liang^{#1}, Jiancong Zhang^{#1}, Karthick Ramalingam^{1,2}, Qiang Wei¹, Kwan San Hui³, Su Htike Aung⁴, Kwun Nam Hui⁵, Fuming Chen^{*1,2}

¹ Guangdong Provincial Key Laboratory of Quantum Engineering and Quantum Materials, Guangdong Engineering Technology Research Center of Efficient Green Energy and Environment Protection Materials, School of Physics and Telecommunication Engineering, South China Normal University, Guangzhou 510006, P.R. China

² School of Electronic and Information Engineering, South China Normal University, Foshan, 528225, P.R. China

³ Engineering, Faculty of Science, University of East Anglia, Norwich, UK

⁴ Department of Physics, Materials Research Laboratory, University of Mandalay, 05032, Mandalay, Myanmar

⁵ Joint Key Laboratory of the Ministry of Education, Institute of Applied Physics and Materials Engineering, University of Macau, Avenida da Universidade, Taipa, Macau, PR China

E-mail addresses: fmchen@m.scnu.edu.cn (F. C.)

these authors contributed equally

Abstract: Herein, we propose a stable and efficient photo-driven electrochemical desalination technique without any electrical. The whole desalination process is driven by CdS quantum dots (QDs) sensitized BiVO₄ photoanode, where I⁻/I⁻-3 redox couples are recirculated as the electrolyte. Two salt streams are sandwiched between the photoanode and cathode. The salt ions in desalted stream are continuously extracted by the redox reaction of I⁻/I⁻-3 electrolyte at their respective electrode chambers. The initial photocurrent of 2.58 mA/cm² can be obtained in the present photoanode-assisted desalination device, which is much greater than the previous reported results. Besides,

the electrical current of the photo-electricity conversion system is extremely stable in the current system. Within the four batch cycles, the variation of salt removal rate is as low as $2.3 \mu\text{g}/(\text{cm}^2 \cdot \text{min})$ without significant decay. The photoanode-electrolyte interface, charge separation and transportation are further investigated by photoluminescence, electrochemical impedance spectroscopy and Mott-Schottky analysis. The promising desalination performance can be attributed to the synergistic effect of CdS QDs and BiVO_4 heterojunction which is applied in the field of solar-driven desalination for the first time. This work is significant for the design of high light-absorbing heterojunction photocatalysts for the dual functions of energy production and water desalination.

Keywords: Photo-electrochemical desalination, CdS QDs/ BiVO_4 , photoanode, energy consumption.

1. Introduction

The water scarcity has become a global problem since the 21st century[1-4]. One-third of the world's population still survives at the area with the insufficient drinking water[5-7]. However, 71% of Earth's surface is covered by water and 97 % of water amount is located at ocean. Seawater desalination is the unique route to solve the problem of water shortage[8-10]. Typically, there are several desalination technologies such as multi-effect distillation (MED), multi-stage flash (MSF), reverse osmosis (RO), capacitive deionization (CDI) etc[11-20]. However, the operating costs of these techniques are relatively high, of which approximate 50% is attributed to the energy

consumption[21-23]. In this case, it will be important to utilize the renewable energy sources as the desalination operation[21, 24, 25]. The solar energy is considered to be an inexhaustible and renewable resource that has been widely studied[26, 27]. For example, the solar-powered reverse osmosis (S-RO) is a mature commercial technology, where the RO system is operated by the power obtained from solar panels which are externally interconnected [28-31]. In nature, the solar power supplies the electrical energy via the photo-electricity conversion to drive the RO process. The cost in S-RO systems is highly site-dependent[29]. In the other way, the thermal distillation desalination is operated by the heat from solar energy[32]. Whereas this system is not applied for the large-scale desalination.

In recent times, a new era of photo-electrochemical desalination technology has been emerging, where the photoelectric conversion electrode is integrated into the electrochemical desalination device[33-36]. For instance, Liang et al. proposed a photo-microbial desalination method based on bio-photocatalyst anode[37]. However, the bacteria anode is very sensitive to the environment, which limits its practical application. More recently, Kim et al. proposed a ternary hybrid solar desalination process[38], which possesses the three-in-one functions of desalination, photo-electrocatalytic water treatment and hydrogen production within a single device. The desalination of brackish water is triggered by the photo-induced charge carriers generated by TiO₂ nanoarray photoanodes, and the desalted ions in the saline water are transferred into electrolytes with the hydrogen evolution at the cathode. However, the system is still suffered from chloride ion oxidation and the declined efficiency. In our previous work, we reported a

similar two-electrode continuous desalination device where LEG4/TiO₂ (LEG4, a kind of 2-Propenoic acid dye) was used as photoanode, Pt-coated graphite as cathode, TEMPO⁺/TEMPO (TEMPO, 4-hydroxy-2,2,6,6-tetramethyl-piperidinoxy) recirculation as electrolyte between photoanode and cathode[33]. Whereas a very low initial photocurrent of 0.31 mA/cm² results in a limited desalination performance owing to the weak interface reaction between photoanode and electrolyte. As known, bismuth vanadate (BiVO₄) is a promising visible absorber semiconductor with the advantages of low production cost, high photostability, photocorrosion resistance, narrow band gap (~2.4 eV), and good response to visible light excitation[39-42]. Unfortunately, the fast recombination of photo-generated carriers and weak light absorption capacity limit its potential applications[43]. Various approaches have been extensively studied to improve the photoelectricity conversion, including element doping, grain boundary edge modification, QDs sensitized semiconductor etc[44-48]. In particular, QDs-sensitized semiconductors can effectively improve solar energy utilization and charge separation owing to the attractive photosensitizer and tunable band gap[49-51]. Though, polysulfide redox couples have been utilized as conventional redox electrolytes for QDs-sensitized solar cells, the BiVO₄ based photoelectrodes immediately become dark when immersed in solution with polysulfide redox[52]. Moreover, the triiodide/iodide redox couple has larger energy difference with the conduction band edge of BiVO₄ than polysulfide electrolytes, which will lead higher open circuit voltage[53].

In this work, we utilize the combination of CdS/BiVO₄ as photoanode to drive the redox flow electrochemical desalination device with the I⁻/I₃⁻ electrolyte. The high

initial photocurrent density of 2.58 mA/cm^2 is obtained at zero-bias condition. Under light illumination, CdS/BiVO₄ shows the excellent desalination performance compared to the pristine BiVO₄, which may be attributed to the heterostructure effect of CdS QDs and BiVO₄. The coupling of CdS QDs and BiVO₄ not only promotes the quick transportation of carriers, but also facilitates the energy transfer between electrolyte and CdS/BiVO₄ photoanode, which have been proved by photoluminescence, electrochemical impedance spectroscopy, cyclic voltammetry, as well as Mott-Schottky analyses. This highly stable and efficient photoanode-based desalination device plays the dual functions of energy production and water desalination, which is significant for the development of semiconductor materials in the field of solar-driven electrochemical desalination.

2. Experimental section

2.1 Material and the preparation of BiVO₄ film

All chemicals used in this work were of analytical grade and used without any further purification. BiVO₄ film was prepared according to a modified metal-organic decomposition (MOD) method reported in the literature[54, 55]. Firstly, 0.2 M Bi(NO₃)·5H₂O (Aladdin, 99.0%) was dissolved in acetic acid (Damao, ≥99.5%). Then 0.03 M VO(acac)₂ (Aldrich, 98%) and 0.03 M MoO₂(acac)₂ (Aldrich) were dissolved in acetylacetone(Aladdin, 99%). The above solutions were mixed in stoichiometric ratio to form the precursor solution. For Mo doping, Bi:(V+Mo) = 1:1 atomic ratio was applied for 1% Mo: BiVO₄ film. To prepare BiVO₄ film, 70 μL of precursor solution

was dropped on a fluorine doped tin oxide (FTO) glass (2.5 cm×2.5 cm) and dried in Ar atmosphere for 15 min. The dried green transparent precursor film was calcined at 550°C for 30 min to form a yellow BiVO₄ film. The FTO glass used in the experiments was sonically treated by using KOH (0.1 M) in ethanol with ratio of 1:5 for 15 min, then washed with plenty of deionized water and finally stored in acetone for use.

2.2 Hydrogen reduction treatment of BiVO₄ film

The hydrogen reduction treatment of BiVO₄ film by the pyrolysis of NaBH₄ (Aladdin, 98%)[55, 56]. Firstly, 605.28 mg of NaBH₄ was placed into a 15 mL alumina crucible. Then the alumina crucible was covered with the side of FTO coated with BiVO₄ film facing downward. The reaction device was then placed in a 200 mL alumina crucible and covered with an alumina lid. The experimental setup is displayed in **Fig. S1**. Finally, the device was sintered at 500 °C for 30 min. After cooling, the final BiVO₄ film was obtained after the treatment of hydrogen reduction.

2.3 Growth of CdS layer on the BiVO₄ film

In order to enhance the absorption of CdS on the BiVO₄, the hydrogen-treated BiVO₄ was immersed in 0.3 M MPA (solvent is ethanol) and kept at 50 °C for 12 h. Then, CdS quantum dots were deposited on the BiVO₄ film by the successive ionic layer adsorption reaction (SILAR) method[57, 58]. The obtained BiVO₄ film was immersed into 0.5 M CdNO₃·4H₂O (Aladdin, 99%) in ethanol, pure ethanol, 0.5 M Na₂S (Aladdin, 95%) in methanol, and pure methanol for 5 min, 30 s, 5 min, and 30 s, respectively. After cycling the above process for three times, the desired samples were calcined at 300 °C for 2 h.

2.4 Fabrication of the photoanode-assisted electrochemical desalination (PA-ED) device

The PA-ED cell comprised two redox streams (RS), two salt streams (SS), a photoanode and a cathode. The order of these components in this device was as follows:

Photoanode | RS || SS || SS || RS | Cathode

where “|” indicates the separation between the constituent parts, and “||” represents cation exchange membrane (CEM) or anion exchange membrane (AEM).

The two salt streams are separated by an AEM and two CEM membranes are put between the redox stream and salt stream, respectively. The redox electrolyte was a mixture of 0.03 M I₂ (Aladdin, 99%), 1 M NaI (Aladdin, 99.99%) and Guanidine thiocyanate (Aladdin, ≥99%). The total volume of the electrolyte was 5 mL. The redox streams were recirculated by a peristaltic pump. The concentration and volume of NaCl in the two salt chambers were around 7.4 mS/cm and 1.5 mL, respectively. In this apparatus, the thickness of each plate was 3 mm. Each plate has a square of 1 cm² as the active center area. In the experiment, the soft tube with the 1 mm inner diameter was used, and the flow rate was controlled at 2 mL/min.

2.5 Characterization

X-ray diffraction (XRD, BRUKER D8 ADVANCE) was used for structure characterization. The microstructure of the samples was observed by field emission scanning electron microscopy (SEM, ZEISS ULTRAR 55) and high-resolution transmission electron microscopy (HR-TEM, JEM-2100HR 200KV). Raman analysis were collected on the Invia Raman microscope under excitation by 532 nm argon ion

laser. The X-ray photoelectron spectroscopy (XPS, Thermo Scientific™ K-Alpha™) were performed to investigate the chemical states of photo-electrodes. The UV-visible diffuse reflectance spectra (DRS, UV-2600i) was conducted to evaluate the light absorption capacities of photo-electrodes. The photoluminescence (PL, F-4500) spectra was performed to reveal the transfer ability of carriers.

2.6 Electrochemical testing

The measurements of cyclic voltammetry (CV), electrochemical impedance spectroscopy (EIS), Mott-Schottky, linear scanning voltammetry (LSV) and J-V were performed on an electrochemical workstation (CHI760E). The J-V curves were tested by assembling the photo-desalination cells. In CV tests, a conventional three-electrode system was used with the glass carbon as working electrode, platinum sheet counter and Ag/AgCl reference. The I-3/I redox electrolyte is composed of 5 mM LiI (Aladdin, 99%), 0.5 mM I₂ (Aladdin, 99%) and 0.1 M LiClO₄ (Aladdin, 99.99%) in acetonitrile. The EIS and LSV were measured by using a two-electrode configuration under light irradiation as follows:

Photoanode | RS | Cathode

where “|” indicates the separation of the constituent parts. FTO coated with photo-sensitive material was served as photoanode, graphite paper coated with Pt was served as cathode. The electrolyte is flowable between the photoanode and cathode. The test of Mott-Schottky was conducted using the same configuration as EIS and LSV under dark condition. The composition of redox electrolyte was in consistent with the desalination test.

2.7 Characterization of the photo-driven desalination performance

Desalination tests were conducted with a CHI760E electrochemical workstation and the battery analyzer (Neware) at room temperature and a GDM-9061 Multimeter was used to record the photocurrent during the photo-desalination experiments without any external bias. The Xe lamp (LanPu LP-350) was used as the light source to drive the photo-desalination and the TM-207 solar radiation meter was used to evaluate the light intensity. The desalination performance under short-circuit mode and constant current mode was recorded by the electrochemical workstation with the i-t program and a battery analyzer with the v-t program. The peristaltic pumps (Kamoer, LLS PLUS) were used to control the flow rate of the salt chamber and the redox chamber. The conductivity of salt feed was monitored online by the conductivity meters (eDAQ, EPU357).

The salt removal rate (SRR , $\mu\text{g}/(\text{cm}^2 \cdot \text{min})$) presents the desalination ability of PA-ED device per unit of time and active area, which can be calculated through the below equation:

$$SRR = \frac{\left(\frac{\Delta c}{\Delta t} \times V\right)}{A_{cell}}$$

Where $\frac{\Delta c}{\Delta t}$ represents the salt concentration change per minute ($\text{mg}/(\text{L} \cdot \text{min})$), V is the total volume of one salt chamber (mL), and A_{cell} represents the active area of the PA-ED device (cm^2).

The light energy consumption (Ec , $\mu\text{mol}/\text{J}$) is calculated as follows:

$$Ec = \frac{\left(\frac{\Delta c}{\Delta t} \times V\right)}{MM \times P \times A_{cell}}$$

Where MM represents the molar mass of NaCl (58.44 g/mol), P is the specific power of the light (W/cm^2).

3. Results and discussion

The fabrication process of CdS/BiVO₄ photoanode is schematically demonstrated in **Fig. 1a**. Initially, the BiVO₄ thin film was deposited on a fluorine doped tin oxide (FTO) conductive glass by the MOD method, followed by H₂ treatment in the presence of NaBH₄, and then CdS QDs were deposited by the SILAR method and dried in Argon atmosphere. The detailed experiment is described in the experimental section. The measurements of XRD, SEM and HRTEM were performed to investigate the crystal structure, morphology and microstructure of the prepared photoelectrodes. **Fig. 1b** shows the XRD patterns of FTO, BiVO₄ and CdS/BiVO₄. The diffraction peaks of BiVO₄ at 2θ values of 18.7, 28.9, 30.5, 34.5, 35.2, 42.5, 46.7, 47.3 and 53.3° are well indexed to the (101), (112), (004), (200), (020), (015), (204), (024) and (116) planes of the monoclinic phase (JCPDS#83-1699) and the other peaks are indexed to be SnO₂ (JCPDS#88-0287) from the FTO substrate. After depositing CdS QDs, the diffraction peaks are similar with the BiVO₄ because of the low diffraction intensity and small size of CdS QDs. **Fig. 1c** shows the SEM images of olive-like BiVO₄ with an average diameter of ~200 nm, which agrees with the previous reported in literatures[54, 55]. In order to confirm the CdS quantum dots, the sample was subjected to HR-TEM analysis

in **Fig. 1d-f**. It can be clearly seen in **Fig. 1d** that the edges of the olive-like BiVO_4 are wrapped with nanoparticles of CdS QDs. The growth of CdS QDs on the surface of BiVO_4 is clearly visualized with an average diameter between 10-20 nm (**Fig. 1e**). Further, HRTEM lattice of CdS/ BiVO_4 displays two d-spacing values of 0.336 nm and 0.311 nm in **Fig. 1f**, which can be well assigned to (111) plane of CdS QDs (JCPDS#75-1546) and (200) plane of BiVO_4 (JCPDS#83-1699), respectively. Therefore, the result of HRTEM demonstrates that CdS QDs are well anchored on the surface of BiVO_4 by the SILAR method.

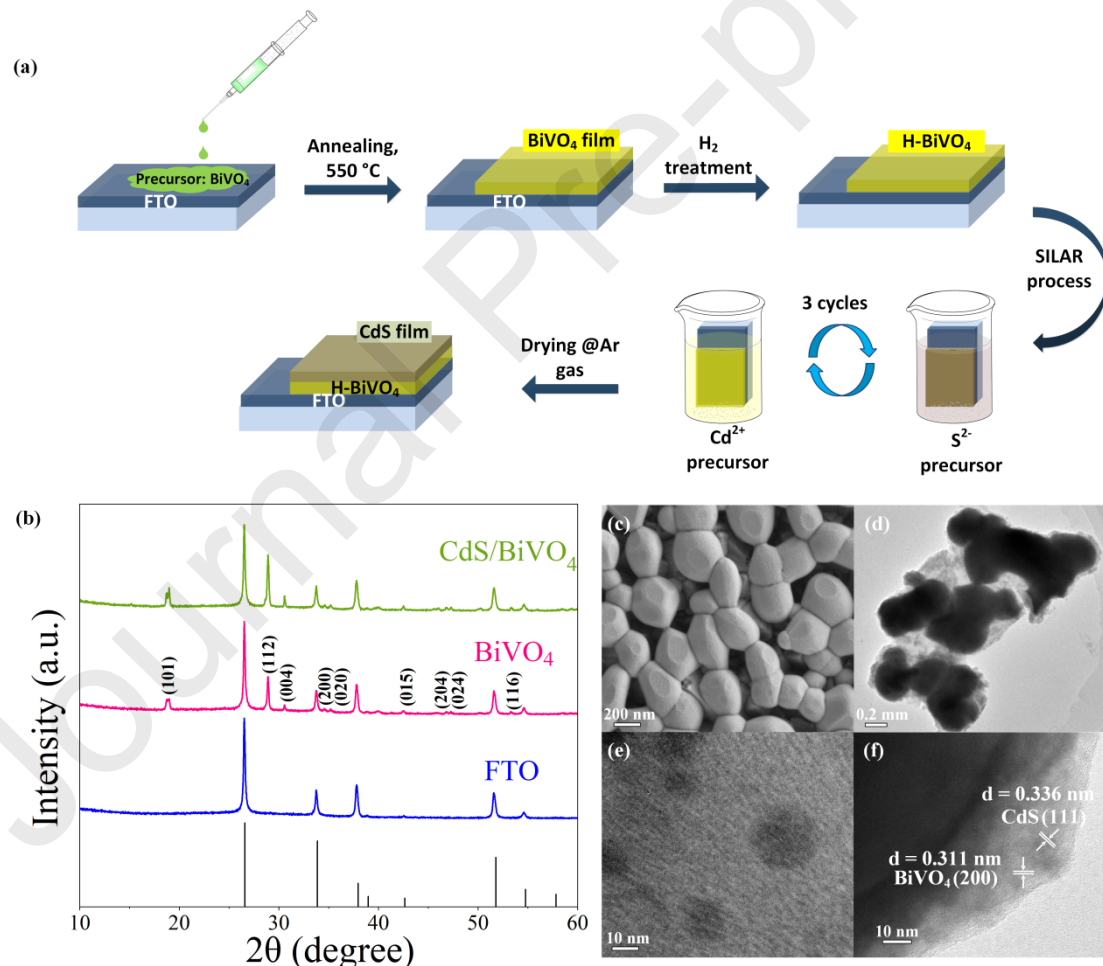


Figure 1: (a) Schematic illustration of the fabrication of CdS/ BiVO_4 photoanodes; (b) XRD patterns of FTO, BiVO_4 and CdS/ BiVO_4 ; (c) SEM of BiVO_4 and (d-f) TEM of

CdS/BiVO₄ photoanode.

As shown in **Fig. S2**, the Raman spectra of all samples show the characteristic vibrational bands of monoclinic BiVO₄. Specifically, the peaks at ~830 and 712 cm⁻¹ correspond to the symmetric (Ag) and asymmetric (Bg) stretching mode of V-O bond[59]. Whereas, the peaks of 327 and 368 cm⁻¹ belong to the Ag and Bg stretching modes of VO₄³⁻, and the other peak at around 212 cm⁻¹ can be attributed to the external mode (rotation/translation)[60]. As seen from the enlarged view of the dominant peak at 830 cm⁻¹ in **Fig. S2b**, after doping with Mo, the Ag mode of V-O bond shifts to lower frequency which is interpreted as an increase of V-O bond lengths by a substitution of Mo for V into the lattice of BiVO₄ [61, 62]. Moreover, the Bg stretching mode of V-O at 712 cm⁻¹ is related to the oxygen vacancies. The peak of H, Mo:BiVO₄ shifts to 718 cm⁻¹ is probably due to the formation of defect states and strain in BiVO₄ after hydrogen treatment[63]. Besides, there occur a peak at around 289 cm⁻¹ in CdS/H, Mo:BiVO₄ which can be assigned to the longitudinal optical phonon (LO) of CdS[64].

To further study the inner influence of H₂ and Mo, XPS characterization is conducted. **Fig. S3a-d** shows the core levels of Bi 4f, V 2p, O 1s and Mo 3d XPS spectra of the samples. The Bi 4f (**Fig. S3a**) and V 2p (**Fig. S3b**) XPS spectra of BiVO₄ exhibit Bi 4f_{5/2} peak at 163.9 eV, Bi 4f_{7/2} peak at 158.6 eV, and V 2p_{1/2} peak at 524.0 eV, V 2p_{3/2} peak at 516.2 eV respectively. After doping with Mo, the binding energy values of Bi 4f and V 2p shift to a higher energy owing to the higher electron negativity of Mo⁶⁺ than V⁵⁺, whereas a lower energy shift is observed by hydrogen treatment owing

to the reduced metal state of Bi^{3+} and V^{5+} [54, 63]. For the fitted O 1s spectra in **Fig. S3c**, two peaks at 529.5 and 531.3 eV can be assigned to the oxygen atoms bound to metals and absorbed oxygen[65, 66]. The hydrogen treatment sample exhibits a relatively higher shift and area for second peak at 531.7 eV (in comparison with the lower intensity peak at 531.3 eV), indicating the presence of more adsorbed oxygen. Since both reduced metal state (Bi^{3+} and V^{5+}) and absorbed oxygen are associated with oxygen vacancies, it indicates the existence of oxygen vacancies in the hydrogenated samples[59, 63, 67, 68]. The successful doping of Mo can be observed in **Fig. S3d**, the binding energy of Mo $3d_{5/2}$ and $3d_{3/2}$ at 231.9 and 235.1 eV are assigned to the Mo^{6+} , indicating that Mo cations are mainly in the form of Mo^{6+} into the lattice of the V places in BiVO_4 [69, 70]. In conclusion, the Raman and XPS characterizations confirm that the Mo doping and hydrogen treatment are beneficial to the enhancement of photoelectrochemical performance.

In prior to perform the desalination test, we also have optimized the optical and electrochemical properties of the photoanodes. The J-V curves of the obtained photoanodes without/with the modification of BiVO_4 were shown in **Fig. 2a**. There is basically no photocurrent can be observed under the dark condition and low photocurrent of $\sim 1.8 \text{ mA/cm}^2$ for the pristine BiVO_4 . Mo doping or Mo doping followed by H_2 treatment could effectively improve the photocurrents to $\sim 2.4 \text{ mA/cm}^2$ and $\sim 2.5 \text{ mA/cm}^2$, respectively. Significantly, the maximum photocurrent was achievable up to $\sim 3.0 \text{ mA/cm}^2$ in CdS/H, Mo: BiVO_4 , which might be attributed to the enhanced light absorption capacity and the charge transfer kinetics between the interface of

photoelectrode and electrolyte. The Mott-Schottky plots were demonstrated to estimate flat-band potentials (E_{fb}) and the donor densities (N_d) of the prepared samples in **Fig. 2b**. All samples exhibit a positive slope, indicating a n-type semiconductor with electrons as the majority carrier. And the E_{fb} are extracted from the intercept at $y=0$, which varies from 0.049, 0.044, 0.030 to -0.006 V vs Ag/AgCl for BiVO₄, Mo:BiVO₄, H, Mo:BiVO₄ and CdS/H, Mo:BiVO₄, respectively. It is obvious that the E_{fb} of the modified materials shift to a negative potential, which indicates the difference between the Fermi level (E_f) of materials and the redox potential increases, resulting in a higher V_{oc} [71]. Besides, the donor densities are calculated using the following equation[56, 72]:

$$N_d = (2/e_0\epsilon\epsilon_0)[d(1/C^2)/dV]^{-1} \quad (1)$$

where e_0 is the electron charge (1.602×10^{-19} C), ϵ is the dielectric constant of BiVO₄ (68)[73], ϵ_0 is the vacuum permittivity (8.854×10^{-14} F cm⁻¹), C is the space charge region capacitance, and V is the applied potential. As expected, the calculated carrier densities follow the order CdS/H, Mo:BiVO₄ (5.27×10^{22} cm⁻³) > H, Mo:BiVO₄ (1.20×10^{22} cm⁻³) > Mo:BiVO₄ (5.15×10^{21} cm⁻³) > BiVO₄ (2.59×10^{21} cm⁻³), further confirming more efficient carrier separation and transfer in the modified photoanode[74].

To determine the light absorption capacity of the bulk-modified film, UV-vis spectra was performed in **Fig. 2c**. All the photoanodes show obvious optical absorption in the range of 300-500 nm. The sample of CdS/H, Mo:BiVO₄ possesses the best optical absorption range of 300-800 nm. The results of the optical absorption of all samples are

consistent with the trend of Mott-Schottky. As shown in **Fig. 2d**, the band gaps of samples can be calculated from the UV-vis absorption spectra according to the below Tauc equation:

$$(\alpha hv)^{1/n} = A(hv - E_g) \quad (2)$$

Where α , hv , A , E_g and n represent the absorption coefficient, photon energy, a proportionality constant, band gap and characteristic of the transition ($n = 1/2$ for direct transition and $n = 2$ for indirect transition) in a semiconductor, respectively. Therefore, the linearity of the Tauc plots of $(\alpha hv)^2$ vs hv allows determination of the optical band gap by the extrapolation of the linear region to the x-axis intercept. Specifically, the band gaps of BiVO₄, Mo: BiVO₄, H, Mo: BiVO₄ and CdS/H, Mo: BiVO₄ are 2.53, 2.51, 2.47 and 2.29 eV, respectively, indicating a reduced band gap and a broaden spectral absorption range.

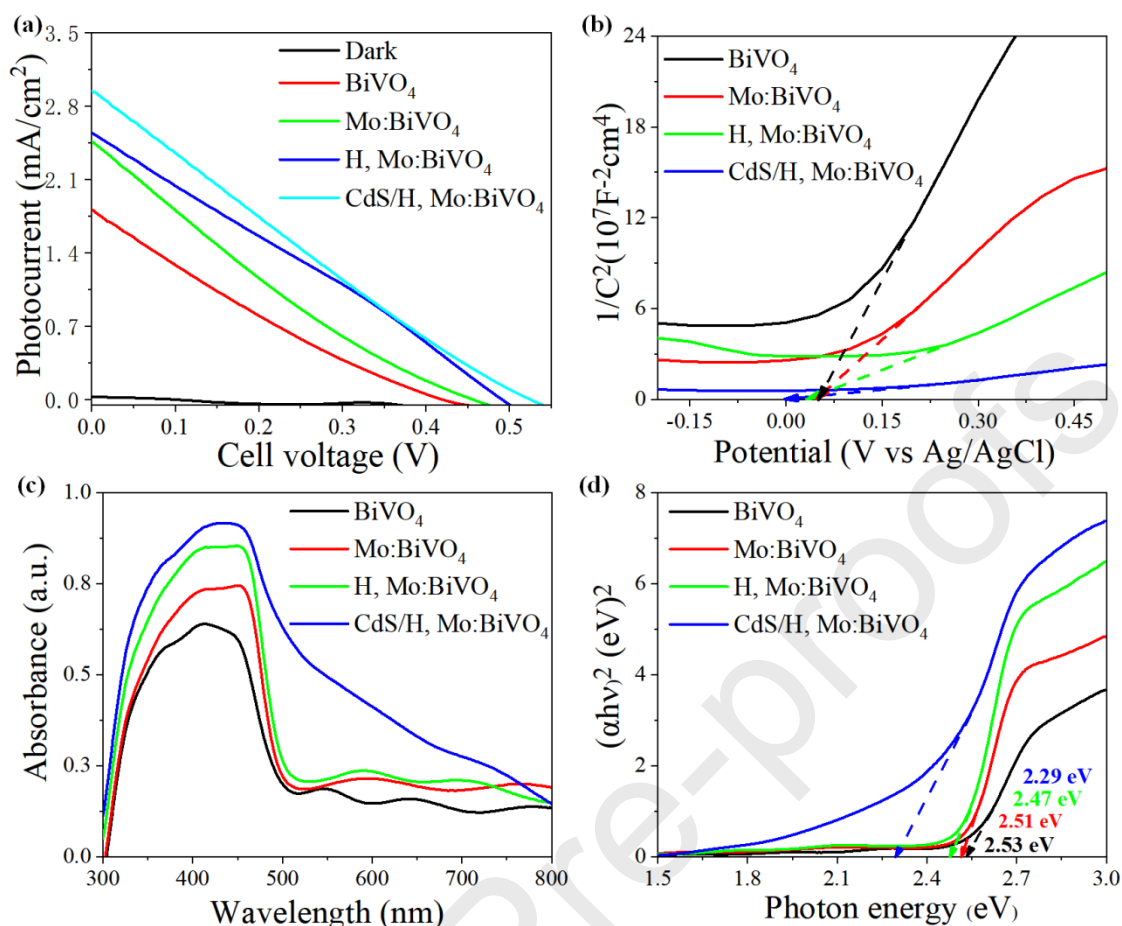


Figure 2: (a) The J-V curves; (b) Mott-Schottky plots; (c) UV-vis spectra and (d) Tauc plots for band gap calculation of the obtained photoanodes.

CdS/H,Mo:BiVO₄ demonstrate the excellent behavior in the optical and electrochemical properties. Thus, it is employed as photoanode for photo-desalination test. The photographs of the PA-ED device components and the setting-up are detailed in Fig. S4 and Fig. S5, respectively. Fig. 3a schematically shows the design and architecture of a two-electrode PA-ED device where the I⁻/I⁻³ redox electrolyte is recirculated between the photoanode and cathode. Two salt streams (stream A and stream B) are flowable between the redox streams. Under illumination, the photo-excited electrons from CdS/BiVO₄ photoanode are transferred to cathode via the

external circuit. The sodium ions are extracted from salt stream B via CEM to the cathode chamber because of the reduction reaction from I-3 to I-. The sodium ions in cathode chamber are recirculated to the anode. Meanwhile, the excited state of CdS/BiVO₄ photoanode is regenerated by the oxidation reaction of I- to I-3 specie, while the sodium ions are released to the salt stream A through CEM. Hence, the salt stream A becomes condensed. As a result, the chloride ions in salt stream B are transported to salt stream A through AEM to compensate the static balance. Therefore, the salt in the stream B is removed with the help of ion exchange membranes by the photo-electrochemical process. To further investigate the enhanced photoelectrochemical performance of CdS QDs/BiVO₄ heterojunction, the band structure and charge transfer mechanism of BiVO₄ and CdS have been carefully analysed. As shown in **Fig. S6a** and **Fig. S6b**, the x-intercepts of CdS and BiVO₄ in Mott-Schottky plots are -0.97 and 0.049 V (vs Ag/AgCl) corresponding to their E_{fb} , which can be converted to be -0.773 and 0.246 V (vs NHE). Theoretically, the conduction band (CB) of n-type semiconductors is 0.2 V more negative than the E_{fb} potential[75] and thus the CB positions of CdS and BiVO₄ are -0.97 and 0.05 V (vs NHE) respectively. Moreover, the band gaps of CdS and BiVO₄ are found to be 2.34 and 2.53 V (vs NHE) according to the Tauc plots in **Fig. S6c** and **Fig. S6d**. Thereafter, the valence band (VB) positions of CdS and BiVO₄ are calculated to be 1.37 and 2.48 V (vs NHE) by using the following equation (3)[76-78]:

$$E_{VB} = E_{CB} - E_g \quad (3)$$

Where E_{VB} , E_{CB} and E_g are VB potential, CB potential and energy band gap of

semiconductors, respectively. Combining the results of Tauc plots and Mott-Schottky plots, the relative position of the VB and the CB of CdS and BiVO₄ are presented in **Fig. S7**. Based on the above experimental results and analysis, the inner transfer mechanism of CdS/BiVO₄ photoanode can be displayed in **Fig. 3b**. Both BiVO₄ and CdS can absorb the sunlight to generate the electron-hole pairs because of their narrow bandgap. Then, the excited electrons are transferred from CB of CdS to CB of BiVO₄ owing to the matched energy level. Consequently, the FTO conducting substrate accepts the electrons to cathode via the outside circuit. Simultaneously, the holes on the VB of BiVO₄ are migrated to the CdS side and regenerated by the oxidation of iodide specie from electrolyte stream, and hence the CdS/BiVO₄ photoanode is reusable.

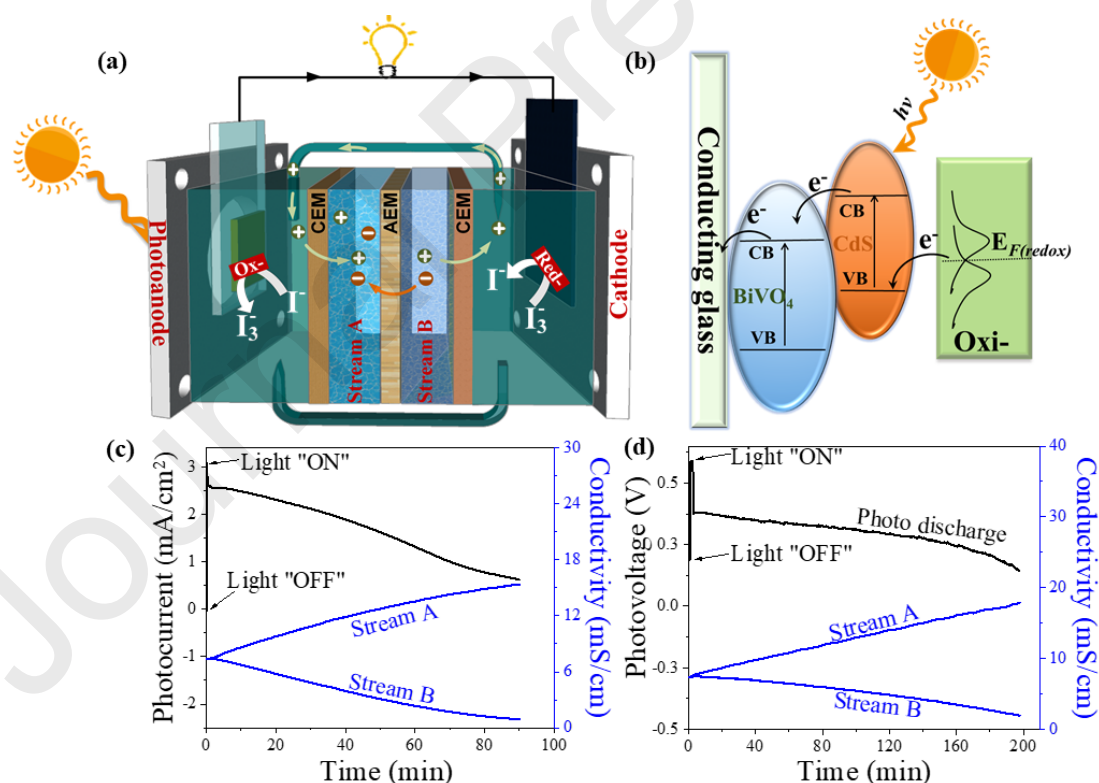
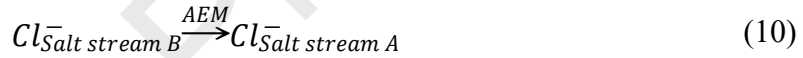
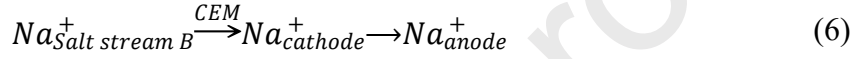
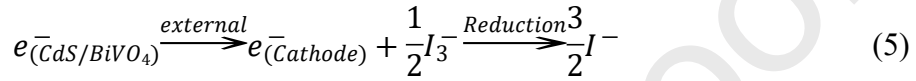
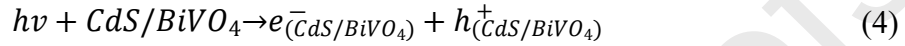


Figure 3: (a) Schematic configuration diagram of desalination mechanism; (b) the inner mechanism of photoanode; (c) photocurrent curve at zero bias (short circuit) under 232 mW/cm² illumination and its corresponding conductivity variation; (d) photo-discharge and its corresponding conductivity variation

curve at 1.0 mA constant current under 232 mW/cm² illumination and its corresponding conductivity variation.

The mechanism of the CdS/BiVO₄ photoanode-based electrochemical desalination is given as follows:



To reveal the electrocatalytic behavior of I⁻/I₃⁻ redox couple, the CV technique was carried out using the electrochemical workstation. As shown in **Fig. S8**, the redox potential of I⁻/I₃⁻ appears at 0.196 V vs. Ag/AgCl. The redox potential and the Fermi level of redox satisfy the transformation of the below equation (9):

$$E_{F, \text{redox}} = -4.5 \text{ eV} - e_o E_{\text{redox}} \quad (11)$$

Where E_{redox} and $E_{F, \text{redox}}$ is the redox potential and the Fermi level of redox species, $e_o = 1$ (electron). Thus, the calculated $E_{F, \text{redox}}$ is -4.696 eV, which lies near the VB of CdS QDs (**Fig. S7**), indicating the feasible energy transfer from electrolyte to the photo-excited electrode material.

In order to explore the importance of CdS/BiVO₄ heterostructure, we compared its photoelectrochemical desalination performance with the bare BiVO₄. Both BiVO₄ and CdS/BiVO₄ can desalinate the brine feed to the freshwater standard (1.0 mS/cm), as shown in **Fig. S9**. The desalination time of CdS/BiVO₄ is much less than that of BiVO₄ photoanode owing to the more efficient photocurrent. The salt removal rate of 58.4 μg/(cm²•min) in CdS/BiVO₄ is higher than 41.9 μg/(cm²•min) in pure BiVO₄. The improvement of the desalination performance may be attributed to the synergetic effect of CdS QDs and olive-like BiVO₄, which not only widens the light response range, but also improves the charge efficiency.

Fig. 3(c-d) demonstrates the desalination performance in the condition of zero bias (short circuit) and constant current. Under the dark condition, the photocurrent is close to zero. Once illuminated, the photocurrent jumps to 3.07 mA/cm² in **Fig. 3c** and then decreases gradually from the initial photocurrent at 2.58 mA/cm² during the continuous desalination. The conductivity in salt stream A increases from the initial 7.36 mS/cm to 15.38 mS/cm while the conductivity in salt stream B decreases to 0.93 mS/cm after 90 minutes. The desalted water can reach the standard of freshwater and the salt removal rate of 57.30 μg/(cm²•min) can be obtained, which is much higher than the previously reports using the two-electrode systems driven by photoanode or photocathode[33, 34]. To measure the short-circuit photocurrent density under a standardized irradiation condition, we adjusted the light source to a sunlight (100 mW/cm²) to test the photo-desalination. **Fig. S10** shows the photocurrent density at zero bias (short circuit) under 100 mW/cm² illumination and its corresponding conductivity variation. Once

illuminated, the initial short-circuit photocurrent density can still reach up to 1.98 mA/cm² and then decreases gradually during the continuous desalination.

Besides, the result under the constant photo-discharge current density (1.0 mA/cm²) was shown in **Fig. 3d**. Under the dark mode, the open-circuit voltage (OCV) is about 0.19 V and increases to 0.59 V once illuminated. Due to the shift of Fermi level, the voltage in CdS/BiVO₄ remains same at open-circuit condition. Once the photo-discharge current applied, the photovoltage immediately drops to 0.38 V and gradually decreases. Simultaneously, the conductivity in salt stream A increases to 17.89 mS/cm from 7.14 mS/cm. At the same time, the conductivity in salt stream B decreases to 1.94 mS/cm after 200 min. The constant salt removal rate is 20.87 μg/(cm²•min) owing to the linearly reduced conductivity. The desalination system is not stable at the initial stage, especially under a short period of time. In the case of long-term photo-driven desalination at zero bias (short circuit) in **Fig. 4c**, the desalination time reaches 46 hours, and thus the variation of conductivity is minor for stream A and stream B. Actually, in the initial stage of short-circuit desalination in **Fig. 4c**, the variation of salt concentration is also unstable. However, with the long desalination process, the change of salt concentration tends to be stable. This discrepancy of variation may be more serious in the small current density. These results are consistent with the previous reported literatures [33, 34]. When doing the light-driven desalination experiment, we measured the pH value of the electrolyte and salt feed for several time periods. The results showed that the pH value of the electrolyte was basically about 5.5, and the pH of the two salt streams was well maintained at neutrality. In order to further confirm that clean fresh

water was obtained, Cd^{2+} in two salt streams were also measured by the inductively coupled plasma optical emission spectroscopy (ICP-OES), and the results showed that Cd was not detected in both salt chambers owing the membrane blocking. Besides, the electrolyte additive about guanidine thiocyanate in streams was tested by the UV-vis spectra with UV absorption at 300 nm. The results showed that the content in the salt stream B was 0.8 ppm and 1.2 ppm in the salt stream A, which are well below than the limit of 5 ppm in drinking water stated by World Health Organization. Even lower amount of guanidine thiocyanate in salt streams is expected when using improved ion-exchange membranes that exhibit better permselectivity. And guanidine thiocyanate has little influence in this work, thus clean fresh water can also be obtained without adding electrolyte additives (**Fig. S11**).

To investigate the controllable dual functions of desalination and energy output in the PA-ED device, the various photo-discharge current densities under 232 mW/cm^2 irradiation was applied, as shown in **Fig. S12a-b**. The photovoltages gradually decrease from the initial 0.45, 0.38 and 0.24 V once the constant currents of 0.5, 1.0 and 1.5 mA are applied, respectively. The rapid salt removal process can be obtained at the high constant current applied. The salt removal rates are calculated to be 6.8, 20.9 and $33.4 \mu\text{g}/(\text{cm}^2 \cdot \text{min})$ at the 0.5, 1.0 and 1.5 mA, respectively, as shown in **Fig. S12c**. Besides, the light energy consumptions are 0.0084, 0.0257 and $0.0410 \mu\text{mol/J}$ at the 0.5, 1.0 and 1.5 mA in **Fig. S12d**, respectively. These results demonstrate that the desalination performance and energy output can be controllable in the PA-ED device.

To demonstrate the influence from light intensity, we adjust the light intensity

from 124 to 305 mW/cm². **Fig. S13a** displays the photocurrent curve and the variation of the salt concentration at zero bias. The high light intensity will result in a rise of photocurrent, indicating a fast salt removal. However, the variation of conductivity curve is not such obvious. The salt removal rates slightly rise with the increased light intensity in **Fig. S13b**. The salt removal rates at 124, 167, 232 and 305 mW/cm² are estimated to be 48.4, 48.8, 49.2 and 49.6 $\mu\text{g}/(\text{cm}^2\cdot\text{min})$, respectively. Furthermore, we have also investigated the influence of light intensity on desalination under same conditions and the results are shown in **Fig. S13c-d**. The photocurrent slightly rises with the increase of light intensity from 124 to 232 mW/cm². Under the light intensity of 232 mW/cm², it takes 94.2 min to reach the level of freshwater in the diluted stream (~ 1 mS/cm). However, 118 min and 130 min in the light intensity of 167 mW/cm² and 124 mW/cm². The photocurrents still remain 0.87 mA, 0.64 mA and 0.62 mA for 232 mW/cm², 167 mW/cm² and 124 mW/cm², respectively, indicating a faster salt feed removal under high light intensity.

The EIS and PL were also carried out to study the charge transfer kinetics and carrier lifetime. **Fig. S14a** shows the Nyquist plots of pristine BiVO₄ and CdS/BiVO₄ under light irradiation at open-circuit voltage. It is clear to see that CdS/BiVO₄ composite exhibits a smaller semi-arc (R_{ct}), implying a lower surface resistance owing to the less charge recombination[79]. The lower PL intensity in **Fig. S14b** of CdS/BiVO₄ also indicates the less recombination of photo-generated electron-hole pairs[80, 81]. These results demonstrate that CdS QDs sensitized BiVO₄ is beneficial to the charge transfer behavior between the interface of photoanode and electrolyte[58].

The stability is a key factor to evaluate the practical feasibility. To explore the long-term stability, the batch cycles of desalination are conducted in **Fig. 4a**. Only the salt streams are replaced without any other change. It can be observed in **Fig. 4a-b** that the photocurrent curves and the concentration variations can be well maintained during the four cycles tests. The salt removal rates shown in **Fig. S15a** are estimated as 57.3, 55.1, 55.0, 56.8 $\mu\text{g}/(\text{cm}^2\cdot\text{min})$, and a small variation is controlled within 2.3 $\mu\text{g}/(\text{cm}^2\cdot\text{min})$. Moreover, the light energy consumptions display little difference in **Fig. S15b**. These results reveal the excellent stability of the current device. The XRD characterization of CdS/BiVO₄ photoanode is displayed in **Fig. S16** before/after the photo desalination. No significant change after the desalination is observed after the cycling desalination, indicating the excellent stability of the electrode material. Further, the long-term stability is demonstrated by increasing the volume of salt streams to 30 mL. As shown in **Fig. 4c**, the salt declines from 7.42 mS/cm to 1.28 mS/cm after the 46-hour irradiation. The photocurrent decreases to 0.26 mA/cm² which can still proceed desalination. The long-term stability test demonstrates that this PA-ED device is also suitable to desalinate the large amount of salt feed for the long time.

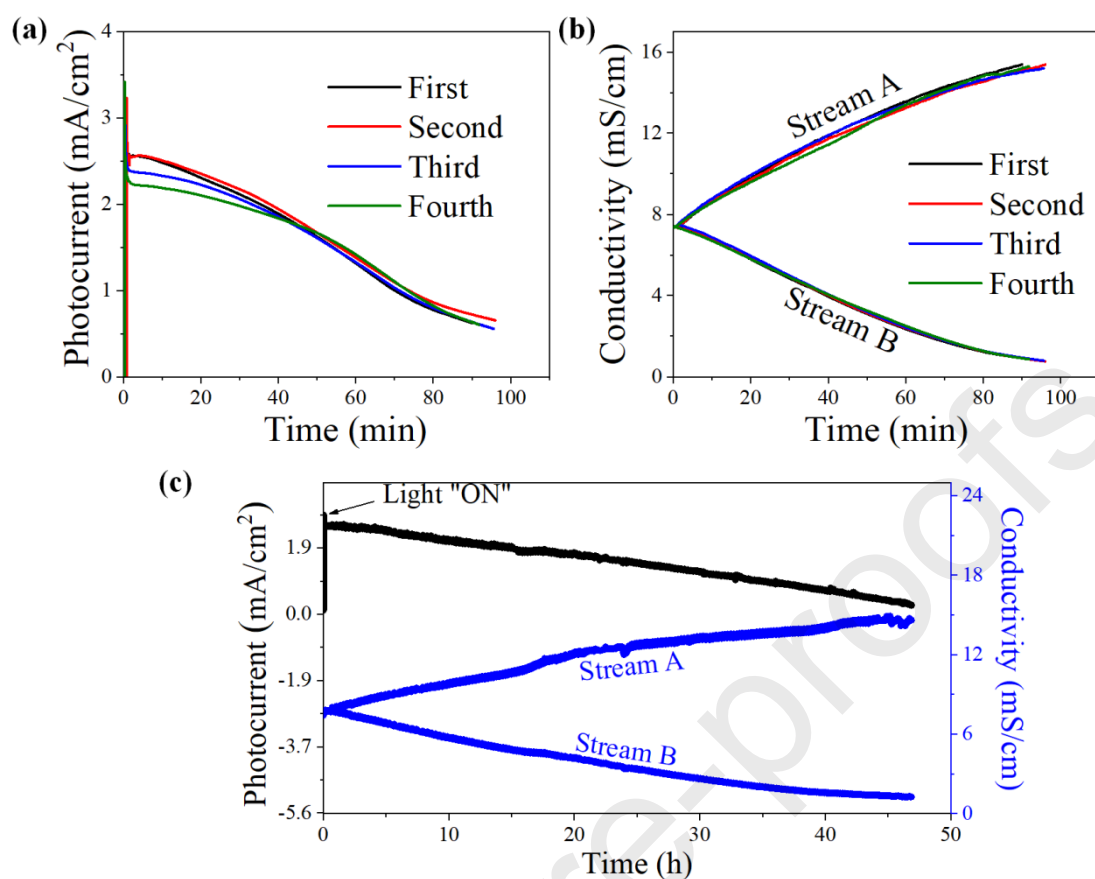


Figure 4: (a) The photocurrent curves at zero bias (short circuit) under 232 mW/cm^2 irradiation for all the cycles (b) the corresponding conductivity variations, and (c) the long-term stability test for PA-ED device under 232 mW/cm^2 irradiation at 30 mL high salt volume.

4. Conclusion

An electrical energy consumption-free photoanode-assisted redox flow electrochemical desalination method was proposed based on CdS QDs/BiVO₄ photoanode. During the photo-desalination process, the I⁻/I³⁻ redox couples are recirculated between the photoanode and cathode to extract the ions from the desalted stream by the redox reaction at their respective electrode channels. Two salt streams

are sandwiched between the photoanode and cathode. The present PA-ED device greatly improves the continuous desalination performance with the initial photocurrent of 2.58 mA/cm^2 under zero-bias condition when compared to the previously reports where the initial photocurrent is as low as 0.31 mA/cm^2 . Moreover, the CdS/BiVO₄ heterostructure exhibits highly improved desalination performance compared to pure BiVO₄, which can be ascribed to the lower recombination rate of charge carriers and the wider solar light absorption range. Besides, the current photo-electricity conversion system possesses excellent stability. Within the four batch cycles of the continuous desalination process, the variation of salt removal rate can be controlled well within $2.3 \mu\text{g}/(\text{cm}^2 \cdot \text{min})$. Through further measurements of PL, EIS and Mott-Schottky, the separation rate and transfer capability of photo-generated carriers are also evaluated. This is the first time that CdS QDs sensitized BiVO₄ photoanode is introduced in the photo-driven electrochemical desalination device, which provides a new idea for the subsequent development of higher-efficiency zero-energy consumption solar-driven desalination.

Acknowledgements

This project was supported by National Key Research and Development Program of China (2019YFE0198000), Science and Technology Program of Guangzhou (No. 2019050001), Education Department of Guangdong Province (2019KZDXM014), Scientific and Technological Plan of Guangdong Province (2018A050506078), SCNU Outstanding Young Scholar Project (8S0256), South China Normal University, the Science and Technology Development Fund, Macau

SAR (File no. 0191/2017/A3, 0041/2019/A1, 0046/2019/AFJ, 0021/2019/AIR), University of Macau (File no. MYRG2017-00216-FST and MYRG2018-00192-IAPME), and the UEA funding. S. H. A. acknowledges the research grant (MYA:01-2020-2021) supported by International Science Program (ISP), Uppsala University, Sweden. F. C. acknowledges the Pearl River Talent Program (2019QN01L951).

Conflict of interest

The authors declare no conflict of interest.

References

- [1] M. Ligaray, N. Kim, S. Park, J.-S. Park, J. Park, Y. Kim, K.H. Cho, Energy projection of the seawater battery desalination system using the reverse osmosis system analysis model, *Chemical Engineering Journal* 395 (2020) 125082. <https://doi.org/10.1016/j.cej.2020.125082>.
- [2] O. Bozorg-Haddad, B. Zolghadr-Asli, P. Sarzaeim, M. Aboutalebi, X. Chu, H.A. Loáiciga, Evaluation of water shortage crisis in the Middle East and possible remedies, *Journal of Water Supply: Research and Technology-Aqua* 69(1) (2019) 85-98. <https://doi.org/10.2166/aqua.2019.049>.
- [3] M. Gao, L. Zhu, C.K. Peh, G.W. Ho, Solar absorber material and system designs for photothermal water vaporization towards clean water and energy production, *Energy & Environmental Science* 12(3) (2019) 841-864. <https://doi.org/10.1039/C8EE01146J>.
- [4] L. Zhu, M. Gao, C.K.N. Peh, G.W. Ho, Recent progress in solar-driven interfacial water evaporation: Advanced designs and applications, *Nano Energy* 57 (2019) 507-518.

<https://doi.org/10.1016/j.nanoen.2018.12.046>.

[5] N. Abdullah, N. Yusof, A.F. Ismail, W.J. Lau, Insights into metal-organic frameworks-integrated membranes for desalination process: A review, *Desalination* 500 (2021) 114867.

<https://doi.org/10.1016/j.desal.2020.114867>.

[6] P.S. Goh, A.F. Ismail, A review on inorganic membranes for desalination and wastewater treatment, *Desalination* 434 (2018) 60-80. <https://doi.org/10.1016/j.desal.2017.07.023>.

[7] M.M. Mekonnen, A.Y. Hoekstra, Four billion people facing severe water scarcity, *Science Advances* 2(2) (2016) e1500323. <https://doi.org/10.1126/sciadv.1500323>.

[8] J. Wang, J. Dai, Z. Jiang, B. Chu, F. Chen, Recent progress and prospect of flow-electrode electrochemical desalination system, *Desalination* 504 (2021) 114964.

<https://doi.org/10.1016/j.desal.2021.114964>.

[9] V.G. Gude, Desalination and sustainability – An appraisal and current perspective, *Water Research* 89 (2016) 87-106. <https://doi.org/10.1016/j.watres.2015.11.012>.

[10] J.R. Ziolkowska, R. Reyes, Impact of socio-economic growth on desalination in the US, *Journal of Environmental Management* 167 (2016) 15-22.

<https://doi.org/10.1016/j.jenvman.2015.11.013>.

[11] J. Jawad, A.H. Hawari, S. Javaid Zaidi, Artificial neural network modeling of wastewater treatment and desalination using membrane processes: A review, *Chemical Engineering Journal* 419 (2021) 129540. <https://doi.org/10.1016/j.cej.2021.129540>.

[12] J. Choi, P. Dorji, H.K. Shon, S. Hong, Applications of capacitive deionization: Desalination, softening, selective removal, and energy efficiency, *Desalination* 449 (2019) 118-130.

<https://doi.org/10.1016/j.desal.2018.10.013>.

- [13] F. Chen, J. Wang, C. Feng, J. Ma, T. David Waite, Low energy consumption and mechanism study of redox flow desalination, *Chemical Engineering Journal* 401 (2020) 126111. <https://doi.org/10.1016/j.cej.2020.126111>.
- [14] Q. Wei, Y. Hu, J. Wang, Q. Ru, X. Hou, L. Zhao, D.Y.W. Yu, K. San Hui, D. Yan, K.N. Hui, F. Chen, Low energy consumption flow capacitive deionization with a combination of redox couples and carbon slurry, *Carbon* 170 (2020) 487-492. <https://doi.org/10.1016/j.carbon.2020.07.044>.
- [15] S. Lin, H. Zhao, L. Zhu, T. He, S. Chen, C. Gao, L. Zhang, Seawater desalination technology and engineering in China: A review, *Desalination* 498 (2021) 114728. <https://doi.org/10.1016/j.desal.2020.114728>.
- [16] F.E. Ahmed, B.S. Lalia, R. Hashaikh, N. Hilal, Alternative heating techniques in membrane distillation: A review, *Desalination* 496 (2020) 114713. <https://doi.org/10.1016/j.desal.2020.114713>.
- [17] J. Ravi, M.H.D. Othman, T. Matsuura, M. Ro'il Bilad, T.H. El-badawy, F. Aziz, A.F. Ismail, M.A. Rahman, J. Jaafar, Polymeric membranes for desalination using membrane distillation: A review, *Desalination* 490 (2020) 114530. <https://doi.org/10.1016/j.desal.2020.114530>.
- [18] S. Zhao, Z. Liao, A. Fane, J. Li, C. Tang, C. Zheng, J. Lin, L. Kong, Engineering antifouling reverse osmosis membranes: A review, *Desalination* 499 (2021) 114857. <https://doi.org/10.1016/j.desal.2020.114857>.
- [19] B. Al-Najar, C.D. Peters, H. Albuflasa, N.P. Hankins, Pressure and osmotically driven membrane processes: A review of the benefits and production of nano-enhanced membranes for desalination, *Desalination* 479 (2020) 114323. <https://doi.org/10.1016/j.desal.2020.114323>.

- [20] W. Xing, J. Liang, W. Tang, D. He, M. Yan, X. Wang, Y. Luo, N. Tang, M. Huang, Versatile applications of capacitive deionization (CDI)-based technologies, *Desalination* 482 (2020) 114390. <https://doi.org/10.1016/j.desal.2020.114390>.
- [21] H. Nassrullah, S.F. Anis, R. Hashaikeh, N. Hilal, Energy for desalination: A state-of-the-art review, *Desalination* 491 (2020) 114569. <https://doi.org/10.1016/j.desal.2020.114569>.
- [22] S. Burn, M. Hoang, D. Zarzo, F. Olewniak, E. Campos, B. Bolto, O. Barron, Desalination techniques — A review of the opportunities for desalination in agriculture, *Desalination* 364 (2015) 2-16. <https://doi.org/10.1016/j.desal.2015.01.041>.
- [23] J. Schallenberg-Rodríguez, J.M. Veza, A. Blanco-Marigorta, Energy efficiency and desalination in the Canary Islands, *Renewable and Sustainable Energy Reviews* 40 (2014) 741-748. <https://doi.org/10.1016/j.rser.2014.07.213>.
- [24] Y. Wu, Z. Tian, S. Yuan, Z. Qi, Y. Feng, Y. Wang, R. Huang, Y. Zhao, J. Sun, W. Zhao, W. Guo, J. Feng, J. Sun, Solar-driven self-powered alkaline seawater electrolysis via multifunctional earth-abundant heterostructures, *Chemical Engineering Journal* 411 (2021) 128538. <https://doi.org/10.1016/j.cej.2021.128538>.
- [25] J. Dai, M. Huang, K.S. Hui, D.Y.W. Yu, D. Yan, K.N. Hui, S.C. Tan, L. Zhang, F. Chen, Redox flow desalination based on the temperature difference as a driving force, *Chemical Engineering Journal* 416 (2021) 127716. <https://doi.org/10.1016/j.cej.2020.127716>.
- [26] L. Fu, H. Li, L. Wang, R. Yin, B. Li, L. Yin, Defect passivation strategies in perovskites for an enhanced photovoltaic performance, *Energy & Environmental Science* 13(11) (2020) 4017-4056. <https://doi.org/10.1039/d0ee01767a>.
- [27] D. Zhu, G. Huang, L. Zhang, Y. He, H. Xie, W. Yu, Silver Nanowires Contained Nanofluids

with Enhanced Optical Absorption and Thermal Transportation Properties, *Energy & Environmental Materials* 2(1) (2019) 22-29. <https://doi.org/10.1002/eem2.12027>.

[28] M. Freire-Gormaly, A.M. Bilton, Design of photovoltaic powered reverse osmosis desalination systems considering membrane fouling caused by intermittent operation, *Renewable Energy* 135 (2019) 108-121. <https://doi.org/10.1016/j.renene.2018.11.065>.

[29] M.T. Mito, X. Ma, H. Albuflasa, P.A. Davies, Reverse osmosis (RO) membrane desalination driven by wind and solar photovoltaic (PV) energy: State of the art and challenges for large-scale implementation, *Renewable and Sustainable Energy Reviews* 112 (2019) 669-685. <https://doi.org/10.1016/j.rser.2019.06.008>.

[30] F.E. Ahmed, R. Hashaikeh, N. Hilal, Solar powered desalination – Technology, energy and future outlook, *Desalination* 453 (2019) 54-76. <https://doi.org/10.1016/j.desal.2018.12.002>.

[31] E.J. Okampo, N. Nwulu, Optimisation of renewable energy powered reverse osmosis desalination systems: A state-of-the-art review, *Renewable and Sustainable Energy Reviews* 140 (2021) 110712. <https://doi.org/10.1016/j.rser.2021.110712>.

[32] A. Giwa, A. Yusuf, A. Dindi, H.A. Balogun, Polygeneration in desalination by photovoltaic thermal systems: A comprehensive review, *Renewable and Sustainable Energy Reviews* 130 (2020) 109946. <https://doi.org/10.1016/j.rser.2020.109946>.

[33] F. Chen, R. Karthick, Q. Zhang, J. Wang, M. Liang, J. Dai, X. Jiang, Y. Jiang, Exploration of a photo-redox desalination generator, *Journal of Materials Chemistry A* 7(35) (2019) 20169-20175. <https://doi.org/10.1039/c9ta06307b>.

[34] M. Liang, K. Feng, R. Karthick, L. Zhang, Y. Shi, K.S. Hui, K.N. Hui, F. Jiang, F. Chen, Photocathode-assisted redox flow desalination, *Green Chemistry* 22 (2020) 4133-4139.

<https://doi.org/10.1039/d0gc01191f>.

[35] K. Ramalingam, Q. Wei, F. Chen, K. Shen, M. Liang, J. Dai, X. Hou, Q. Ru, G. Babu, Q. He, P.M. Ajayan, Achieving High-Quality Freshwater from a Self-Sustainable Integrated Solar Redox-Flow Desalination Device, *Small* 17(30) (2021) 2100490.

<https://doi.org/10.1002/smll.202100490>.

[36] K. Ramalingam, M. Liang, N.L.W. Pyae, S.H. Aung, T.Z. Oo, P. Srimuk, J. Ma, V. Presser, F. Chen, T.D. Waite, Self-Sustained Visible-Light-Driven Electrochemical Redox Desalination, *ACS Applied Materials & Interfaces* 12(29) (2020) 32788-32796.

<https://doi.org/10.1021/acsami.0c08286>.

[37] Y. Liang, H. Feng, D. Shen, N. Li, Y. Long, Y. Zhou, Y. Gu, X. Ying, Q. Dai, A high-performance photo-microbial desalination cell, *Electrochimica Acta* 202 (2016) 197-202.

<https://doi.org/10.1016/j.electacta.2016.03.177>.

[38] S. Kim, D.S. Han, H. Park, Reduced titania nanorods and Ni–Mo–S catalysts for photoelectrocatalytic water treatment and hydrogen production coupled with desalination, *Applied Catalysis B: Environmental* 284 (2021) 119745.

<https://doi.org/10.1016/j.apcatb.2020.119745>.

[39] B. Baral, K. Parida, {040/110} Facet Isotype Heterojunctions with Monoclinic Scheelite BiVO₄, *Inorganic Chemistry* 59(14) (2020) 10328-10342.

<https://doi.org/10.1021/acs.inorgchem.0c01465>.

[40] M. A. M. J. M. Ashokkumar, P. Arunachalam, A review on BiVO₄ photocatalyst: Activity enhancement methods for solar photocatalytic applications, *Applied Catalysis A: General* 555 (2018) 47-74. <https://doi.org/10.1016/j.apcata.2018.02.010>.

- [41] H. She, P. Yue, J. Huang, L. Wang, Q. Wang, One-step hydrothermal deposition of F:FeOOH onto BiVO₄ photoanode for enhanced water oxidation, *Chemical Engineering Journal* 392 (2020) 123703. <https://doi.org/10.1016/j.cej.2019.123703>.
- [42] Y. Gao, G. Yang, Y. Dai, X. Li, J. Gao, N. Li, P. Qiu, L. Ge, Electrodeposited Co-Substituted LaFeO₃ for Enhancing the Photoelectrochemical Activity of BiVO₄, *ACS Applied Materials & Interfaces* 12(15) (2020) 17364-17375. <https://doi.org/10.1021/acsami.9b21386>.
- [43] H. Yang, B. Xu, Q. Zhang, S. Yuan, Z. Zhang, Y. Liu, Z. Nan, M. Zhang, T. Ohno, Boosting visible-light-driven photocatalytic performance of waxberry-like CeO₂ by samarium doping and silver QDs anchoring, *Applied Catalysis B: Environmental* 286 (2021) 119845. <https://doi.org/10.1016/j.apcatb.2020.119845>.
- [44] S. Zhou, R. Tang, L. Yin, Slow-Photon-Effect-Induced Photoelectrical-Conversion Efficiency Enhancement for Carbon-Quantum-Dot-Sensitized Inorganic CsPbBr₃ Inverse Opal Perovskite Solar Cells, *Advanced Materials* 29(43) (2017) 1703682. <https://doi.org/10.1002/adma.201703682>.
- [45] X. Wang, Z. Li, Z. Zhang, Q. Li, E. Guo, C. Wang, L. Yin, Mo-doped SnO₂ mesoporous hollow structured spheres as anode materials for high-performance lithium ion batteries, *Nanoscale* 7(8) (2015) 3604-13. <https://doi.org/10.1039/c4nr05789a>.
- [46] F. Raziq, A. Hayat, M. Humayun, S.K. Baburao Mane, M.B. Faheem, A. Ali, Y. Zhao, S. Han, C. Cai, W. Li, D.-C. Qi, J. Yi, X. Yu, M.B.H. Breese, F. Hassan, F. Ali, A. Mavlonov, K. Dhanabalan, X. Xiang, X. Zu, S. Li, L. Qiao, Photocatalytic solar fuel production and environmental remediation through experimental and DFT based research on CdSe-QDs-coupled P-doped-g-C₃N₄ composites, *Applied Catalysis B: Environmental* 270 (2020) 118867.

<https://doi.org/10.1016/j.apcatb.2020.118867>.

[47] H. Ma, Y. He, X. Li, J. Sheng, J. Li, F. Dong, Y. Sun, In situ loading of MoO₃ clusters on ultrathin Bi₂MoO₆ nanosheets for synergistically enhanced photocatalytic NO abatement, *Applied Catalysis B: Environmental* 292 (2021) 120159.

<https://doi.org/10.1016/j.apcatb.2021.120159>.

[48] K. Lin, L. Feng, D. Li, J. Zhang, W. Wang, B. Ma, Improved photocatalytic hydrogen evolution on (Ru/WC)/CdS via modulating the transferring paths of photo-excited electrons, *Applied Catalysis B: Environmental* 286 (2021) 119880.

<https://doi.org/10.1016/j.apcatb.2021.119880>.

[49] D. Kandi, S. Martha, A. Thirumurugan, K.M. Parida, CdS QDs-Decorated Self-Doped γ -Bi₂MoO₆: A Sustainable and Versatile Photocatalyst toward Photoreduction of Cr(VI) and Degradation of Phenol, *ACS Omega* 2(12) (2017) 9040-9056.

<https://doi.org/10.1021/acsomega.7b01250>.

[50] J.-Y. Kim, Y.J. Jang, J. Park, J. Kim, J.S. Kang, D.Y. Chung, Y.-E. Sung, C. Lee, J.S. Lee, M.J. Ko, Highly loaded PbS/Mn-doped CdS quantum dots for dual application in solar-to-electrical and solar-to-chemical energy conversion, *Applied Catalysis B: Environmental* 227 (2018) 409-417. <https://doi.org/10.1016/j.apcatb.2018.01.041>.

[51] S. Zhou, R. Tang, H. Li, L. Fu, B. Li, L. Yin, Fluorescence resonance energy transfer effect enhanced high performance of Si quantum Dots/CsPbBr₃ inverse opal heterostructure perovskite solar cells, *Journal of Power Sources* 439 (2019) 227065.

<https://doi.org/10.1016/j.jpowsour.2019.227065>.

[52] Y. Li, J. Zhu, H. Chu, J. Wei, F. Liu, M. Lv, J. Tang, B. Zhang, J. Yao, Z. Huo, L. Hu, S.

- Dai, BiVO₄ semiconductor sensitized solar cells, *Science China Chemistry* 58(9) (2015) 1489-1493. <https://doi.org/10.1007/s11426-015-5348-3>.
- [53] G. Niu, L. Wang, R. Gao, B. Ma, H. Dong, Y. Qiu, Inorganic iodide ligands in ex situ PbS quantum dot sensitized solar cells with I⁻/I₃⁻ electrolytes, *Journal of Materials Chemistry* 22(33) (2012) 16914-16919. <https://doi.org/10.1039/C2JM32459H>.
- [54] J.H. Kim, Y. Jo, J.H. Kim, J.W. Jang, H.J. Kang, Y.H. Lee, D.S. Kim, Y. Jun, J.S. Lee, Wireless Solar Water Splitting Device with Robust Cobalt-Catalyzed, Dual-Doped BiVO₄ Photoanode and Perovskite Solar Cell in Tandem: A Dual Absorber Artificial Leaf, *ACS Nano* 9(12) (2015) 11820-11829. <https://doi.org/10.1021/acsnano.5b03859>.
- [55] J.H. Kim, J.-W. Jang, Y.H. Jo, F.F. Abdi, Y.H. Lee, R. van de Krol, J.S. Lee, Hetero-type dual photoanodes for unbiased solar water splitting with extended light harvesting, *Nature Communications* 7(1) (2016) 13380. <https://doi.org/10.1038/ncomms13380>.
- [56] M. Li, J. Deng, A. Pu, P. Zhang, H. Zhang, J. Gao, Y. Hao, J. Zhong, X. Sun, Hydrogen-treated hematite nanostructures with low onset potential for highly efficient solar water oxidation, *Journal of Materials Chemistry A* 2(19) (2014) 6727-6733. <https://doi.org/10.1039/C4TA00729H>.
- [57] B.B. Jin, D.J. Wang, S.Y. Kong, G.Q. Zhang, H.S. Huang, Y. Liu, H.Q. Liu, J. Wu, L.H. Zhao, D. He, Voltage-assisted SILAR deposition of CdSe quantum dots into mesoporous TiO₂ film for quantum dot-sensitized solar cells, *Chemical Physics Letters* 735 (2019) 136764. <https://doi.org/10.1016/j.cplett.2019.136764>.
- [58] S. Zhou, L. Yin, CdS quantum dots sensitized mesoporous BiVO₄ heterostructures for solar cells with enhanced photo-electrical conversion efficiency, *Journal of Alloys and*

- Compounds 691 (2017) 1040-1048. <https://doi.org/10.1016/j.jallcom.2016.07.296>.
- [59] H.L. Tan, A. Suyanto, A.T.D. Denko, W.H. Saputera, R. Amal, F.E. Osterloh, Y.H. Ng, Enhancing the Photoactivity of Faceted BiVO₄ via Annealing in Oxygen-Deficient Condition, *Particle & Particle Systems Characterization* 34(4) (2017) 1600290. <https://doi.org/10.1002/ppsc.201600290>.
- [60] M. Li, L. Zhao, L. Guo, Preparation and photoelectrochemical study of BiVO₄ thin films deposited by ultrasonic spray pyrolysis, *International Journal of Hydrogen Energy* 35(13) (2010) 7127-7133. <https://doi.org/10.1016/j.ijhydene.2010.02.026>.
- [61] A. Milbrat, W. Vijselaar, Y. Guo, B. Mei, J. Huskens, G. Mul, Integration of Molybdenum-Doped, Hydrogen-Annealed BiVO₄ with Silicon Microwires for Photoelectrochemical Applications, *ACS Sustainable Chemistry & Engineering* 7(5) (2019) 5034-5044. <https://doi.org/10.1021/acssuschemeng.8b05756>.
- [62] W. Luo, Z. Yang, Z. Li, J. Zhang, J. Liu, Z. Zhao, Z. Wang, S. Yan, T. Yu, Z. Zou, Solar hydrogen generation from seawater with a modified BiVO₄ photoanode, *Energy & Environmental Science* 4(10) (2011) 4046-4051. <https://doi.org/10.1039/C1EE01812D>.
- [63] A.P. Singh, N. Kodan, A. Dey, S. Krishnamurthy, B.R. Mehta, Improvement in the structural, optical, electronic and photoelectrochemical properties of hydrogen treated bismuth vanadate thin films, *International Journal of Hydrogen Energy* 40(12) (2015) 4311-4319. <https://doi.org/10.1016/j.ijhydene.2015.01.085>.
- [64] Z.-J. Li, X.-B. Fan, X.-B. Li, J.-X. Li, F. Zhan, Y. Tao, X. Zhang, Q.-Y. Kong, N.-J. Zhao, J.-P. Zhang, C. Ye, Y.-J. Gao, X.-Z. Wang, Q.-Y. Meng, K. Feng, B. Chen, C.-H. Tung, L.-Z. Wu, Direct synthesis of all-inorganic heterostructured CdSe/CdS QDs in aqueous solution for

improved photocatalytic hydrogen generation, *Journal of Materials Chemistry A* 5(21) (2017) 10365-10373. <https://doi.org/10.1039/c7ta01670k>.

[65] B. Zhang, L. Wang, Y. Zhang, Y. Ding, Y. Bi, Ultrathin FeOOH Nanolayers with Abundant Oxygen Vacancies on BiVO₄ Photoanodes for Efficient Water Oxidation, *Angewandte Chemie* 130(8) (2018) 2270-2274. <https://doi.org/10.1002/ange.201712499>.

[66] B. Baral, D.P. Sahoo, K. Parida, Discriminatory {040}-Reduction Facet/Ag(0) Schottky Barrier Coupled {040/110}-BiVO₄@Ag@CoAl-LDH Z-Scheme Isotype Heterostructure, *Inorganic chemistry* 60(3) (2021) 1698-1715. <https://doi.org/10.1021/acs.inorgchem.0c03210>.

[67] J. Bao, X. Zhang, B. Fan, J. Zhang, M. Zhou, W. Yang, X. Hu, H. Wang, B. Pan, Y. Xie, Ultrathin Spinel-Structured Nanosheets Rich in Oxygen Deficiencies for Enhanced Electrocatalytic Water Oxidation, *Angewandte Chemie International Edition* 54(25) (2015) 7399-7404. <https://doi.org/10.1002/anie.201502226>.

[68] A.H. Elbadawi, L. Ge, J. Zhang, L. Zhuang, S. Liu, X. Tan, S. Wang, Z. Zhu, Partial oxidation of methane to syngas in catalytic membrane reactor: Role of catalyst oxygen vacancies, *Chemical Engineering Journal* 392 (2020) 123739. <https://doi.org/10.1016/j.cej.2019.123739>.

[69] M. Zhou, J. Bao, Y. Xu, J. Zhang, J. Xie, M. Guan, C. Wang, L. Wen, Y. Lei, Y. Xie, Photoelectrodes Based upon Mo:BiVO₄ Inverse Opals for Photoelectrochemical Water Splitting, *ACS Nano* 8(7) (2014) 7088-7098. <https://doi.org/10.1021/nn501996a>.

[70] M. Rohloff, B. Anke, O. Kasian, S. Zhang, M. Lerch, C. Scheu, A. Fischer, Enhanced Photoelectrochemical Water Oxidation Performance by Fluorine Incorporation in BiVO₄ and Mo:BiVO₄ Thin Film Photoanodes, *ACS Applied Materials & Interfaces* 11(18) (2019) 16430-

16442. <https://doi.org/10.1021/acsami.8b16617>.

[71] S. Kundu, P. Sarojinijeeva, R. Karthick, G. Anantharaj, G. Saritha, R. Bera, S. Anandan, A. Patra, P. Ragupathy, M. Selvaraj, D. Jeyakumar, K.V. Pillai, Enhancing the Efficiency of DSSCs by the Modification of TiO₂ Photoanodes using N, F and S, co-doped Graphene Quantum Dots, *Electrochimica Acta* 242 (2017) 337-343. <https://doi.org/10.1016/j.electacta.2017.05.024>.

[72] X. Liu, Y. Yuan, J. Liu, B. Liu, X. Chen, J. Ding, X. Han, Y. Deng, C. Zhong, W. Hu, Utilizing solar energy to improve the oxygen evolution reaction kinetics in zinc–air battery, *Nature Communications* 10(1) (2019) 4767. <https://doi.org/10.1038/s41467-019-12627-2>.

[73] R.P. Antony, P.S. Bassi, F.F. Abdi, S.Y. Chiam, Y. Ren, J. Barber, J.S.C. Loo, L.H. Wong, Electrospun Mo-BiVO₄ for Efficient Photoelectrochemical Water Oxidation: Direct Evidence of Improved Hole Diffusion Length and Charge separation, *Electrochimica Acta* 211 (2016) 173-182. <https://doi.org/10.1016/j.electacta.2016.06.008>.

[74] L. Gao, X. Long, S. Wei, C. Wang, T. Wang, F. Li, Y. Hu, J. Ma, J. Jin, Facile growth of AgVO₃ nanoparticles on Mo-doped BiVO₄ film for enhanced photoelectrochemical water oxidation, *Chemical Engineering Journal* 378 (2019) 122193. <https://doi.org/10.1016/j.cej.2019.122193>.

[75] S. Li, L. Wang, Y. Li, L. Zhang, A. Wang, N. Xiao, Y. Gao, N. Li, W. Song, L. Ge, J. Liu, Novel photocatalyst incorporating Ni-Co layered double hydroxides with P-doped CdS for enhancing photocatalytic activity towards hydrogen evolution, *Applied Catalysis B: Environmental* 254 (2019) 145-155. <https://doi.org/10.1016/j.apcatb.2019.05.001>.

[76] B. Baral, K.H. Reddy, K.M. Parida, Construction of M-BiVO₄/T-BiVO₄ isotype

heterojunction for enhanced photocatalytic degradation of Norfloxacin and Oxygen evolution reaction, *Journal of Colloid and Interface Science* 554 (2019) 278-295.

<https://doi.org/10.1016/j.jcis.2019.07.007>.

[77] M. Liang, C. Zou, W. Wang, Z. Yang, K. Shen, Y. Yang, S. Yang, Bi metal/oxygen-deficient BiO_{2-x} with tetrahedral morphology and high photocatalytic activity, *Nanotechnology* 32(6) (2021) 065702. <https://doi.org/10.1088/1361-6528/abc039>.

[78] N. Li, H. Fan, Y. Dai, J. Kong, L. Ge, Insight into the solar utilization of a novel Z-scheme Cs_{0.33}WO₃/CdS heterostructure for UV-Vis-NIR driven photocatalytic hydrogen evolution, *Applied Surface Science* 508 (2020) 145200. <https://doi.org/10.1016/j.apsusc.2019.145200>.

[79] B. Xu, Y. Li, Y. Gao, S. Liu, D. Lv, S. Zhao, H. Gao, G. Yang, N. Li, L. Ge, Ag-AgI/Bi₃O₄Cl for efficient visible light photocatalytic degradation of methyl orange: The surface plasmon resonance effect of Ag and mechanism insight, *Applied Catalysis B: Environmental* 246 (2019) 140-148. <https://doi.org/10.1016/j.apcatb.2019.01.060>.

[80] A. Behera, D. Kandi, S. Sahoo, K. Parida, Construction of Isoenergetic Band Alignment between CdS QDs and CaFe₂O₄@ZnFe₂O₄ Heterojunction: A Promising Ternary Hybrid toward Norfloxacin Degradation and H₂ Energy Production, *The Journal of Physical Chemistry C* 123(28) (2019) 17112-17126. <https://doi.org/10.1021/acs.jpcc.9b03296>.

[81] S.M. Ghoreishian, K.S. Ranjith, B. Park, S.-K. Hwang, R. Hosseini, R. Behjatmanesh-Ardakani, S.M. Pourmortazavi, H.U. Lee, B. Son, S. Mirsadeghi, Y.-K. Han, Y.S. Huh, Full-spectrum-responsive Bi₂S₃@CdS S-scheme heterostructure with intimate ultrathin RGO toward photocatalytic Cr(VI) reduction and H₂O₂ production: Experimental and DFT studies, *Chemical Engineering Journal* 419 (2021) 129530. <https://doi.org/10.1016/j.cej.2021.129530>.

Journal Pre-proofs

Journal Pre-proofs